S1. NMR and Mass spectra

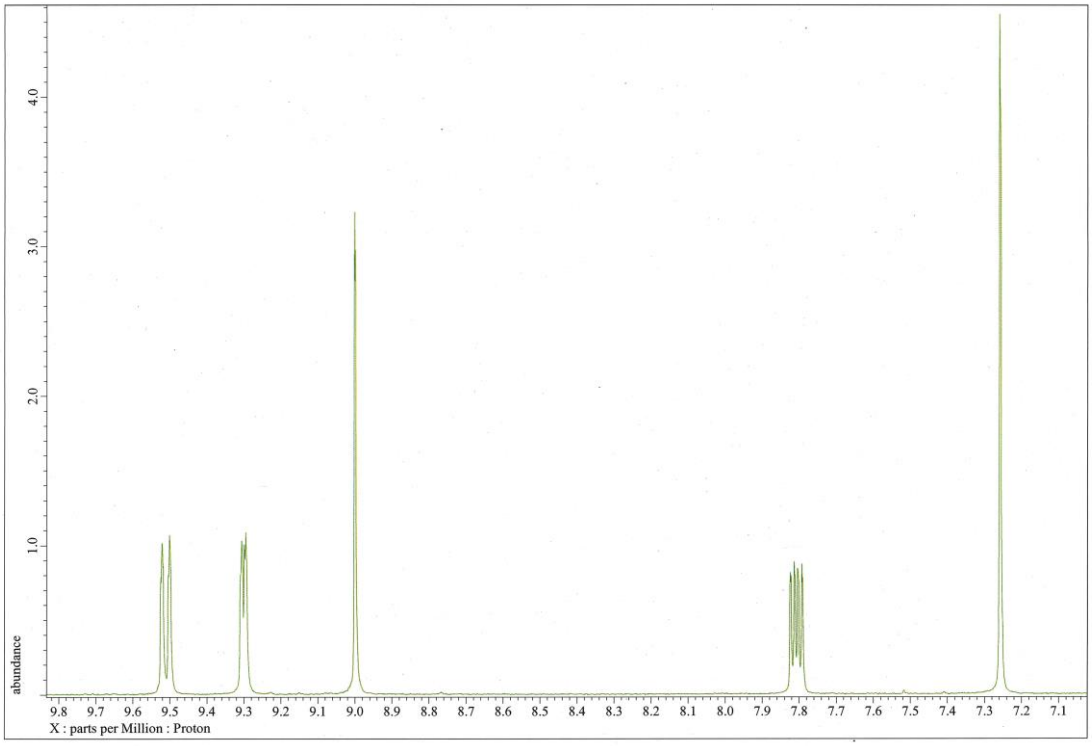

Fig. S1. NMR spectrum of dpq ligand.

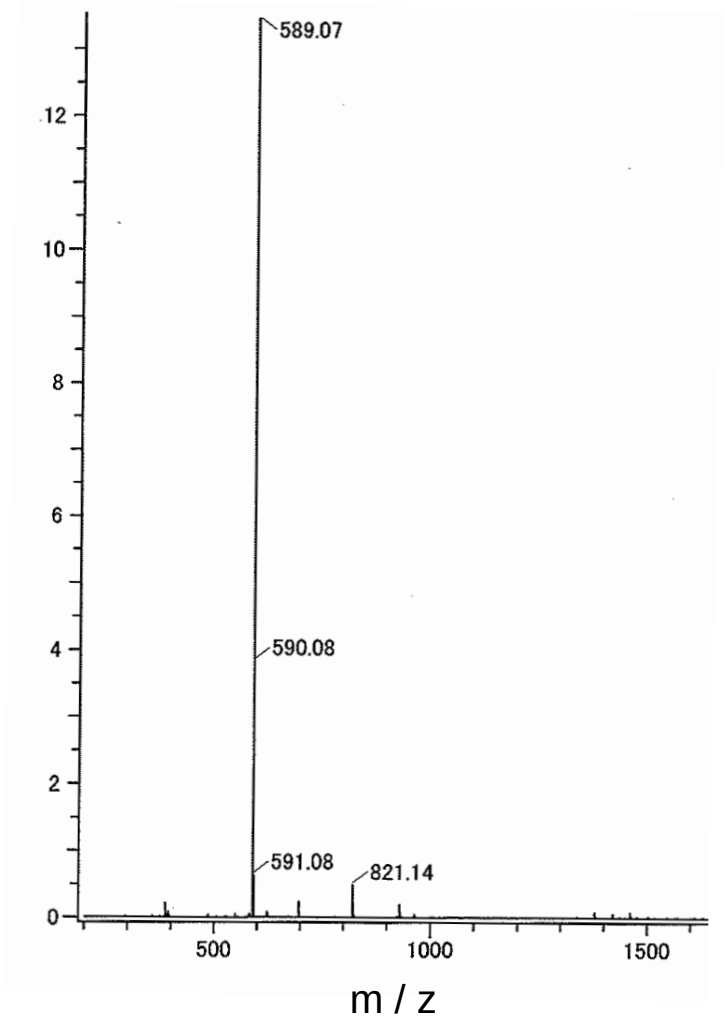

Fig. S2. ESI-Mass spectrum of $Tb(acac)_3dpq$.

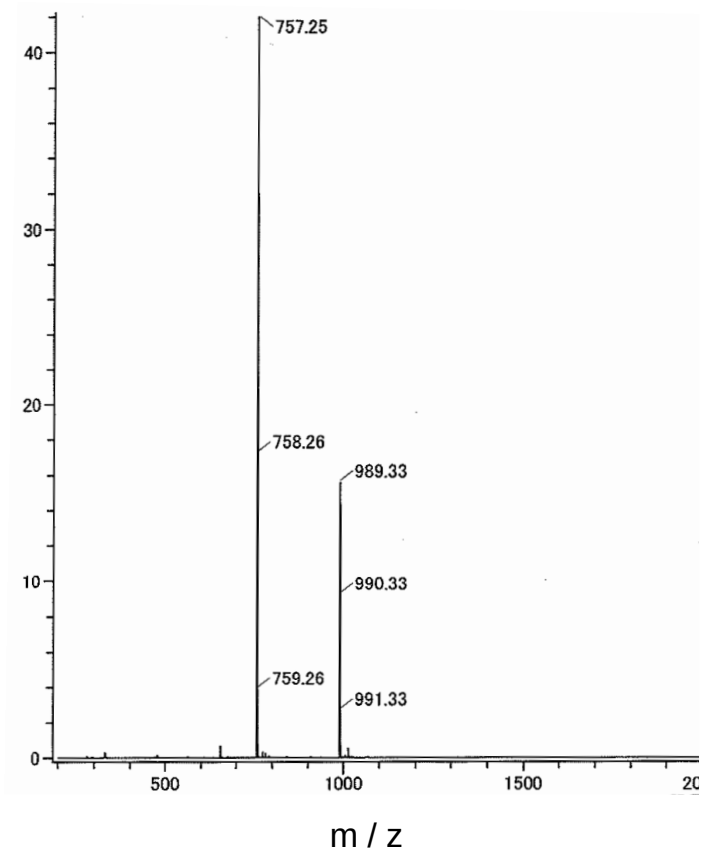

Fig. S3. ESI-Mass spectrum of $Tb(tmh)_3dpq$.

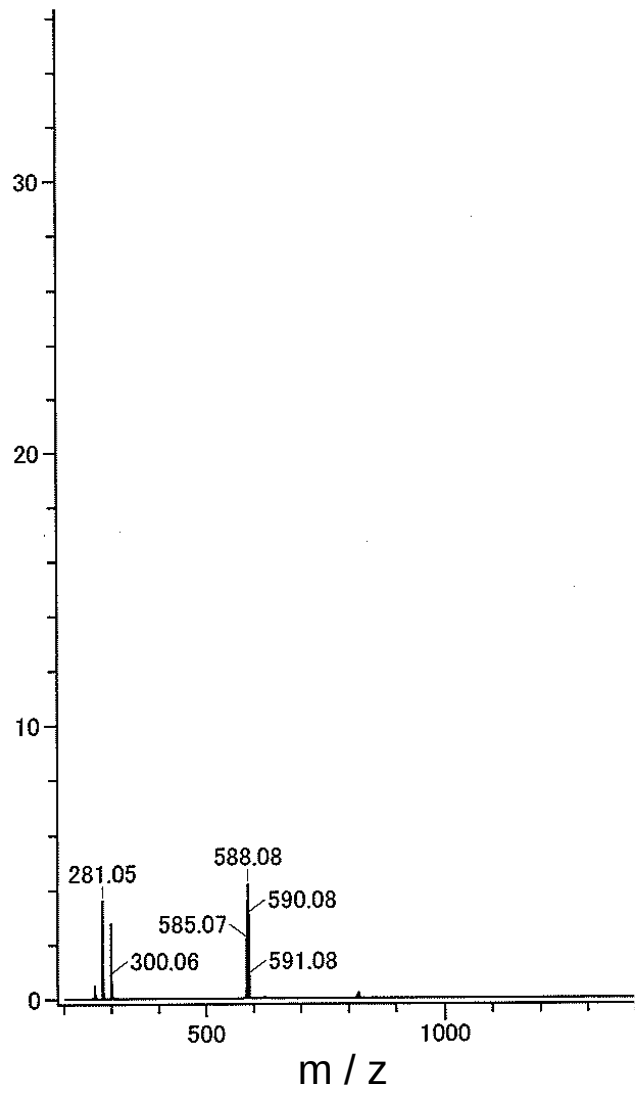

Fig. S4. ESI-Mass spectrum of Gd(acac)$_3$dpq.

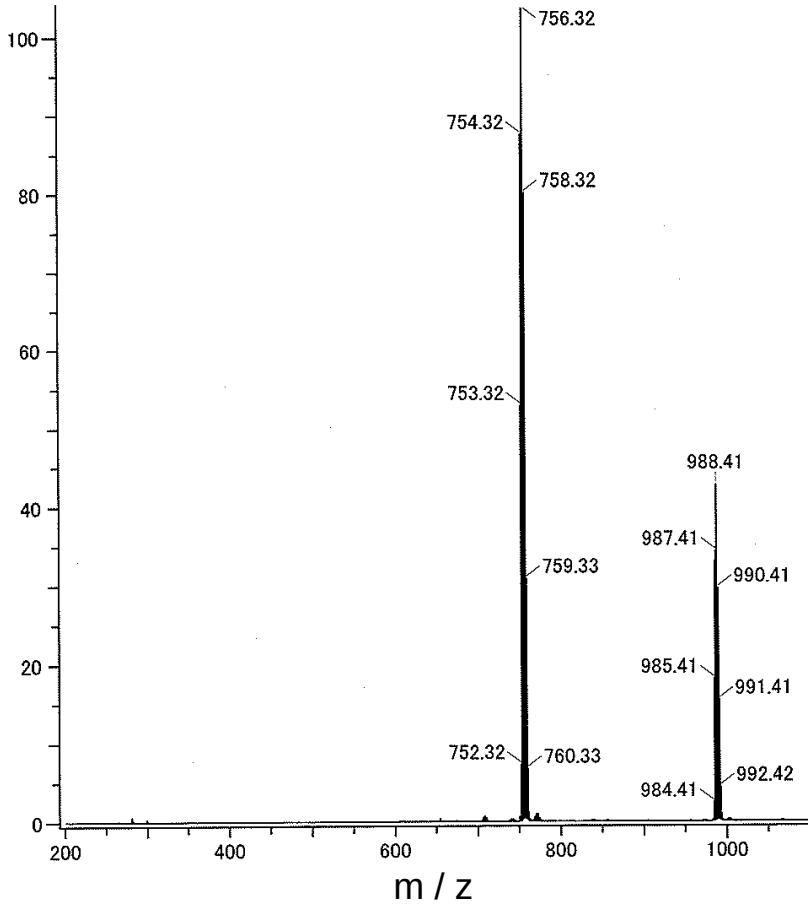

Fig. S5. ESI-Mass spectrum of Gd(tmh)$_3$dpq.

S2. TD-DFT calculations of Tb(III) complexes in isolated states

To clarify the electronic structure of the Tb(III) complexes, we calculated the optimized structure of $Tb(acac)_3dpq$ (PM3) in the isolated state (vacuum condition). The calculations were performed on a simplified model of the Tb(III) unit using a ligand bonded to an Al(III) ion. TD-DFT calculations (CAM-B3LYP/6-31G(d), IPCM-CH_2Cl_2) were then performed for the optimized structure. The calculated T_1 states are mainly composed of LLCT transitions from delocalized orbitals (acac and dpq ligands) to localized orbitals (dpq ligand).

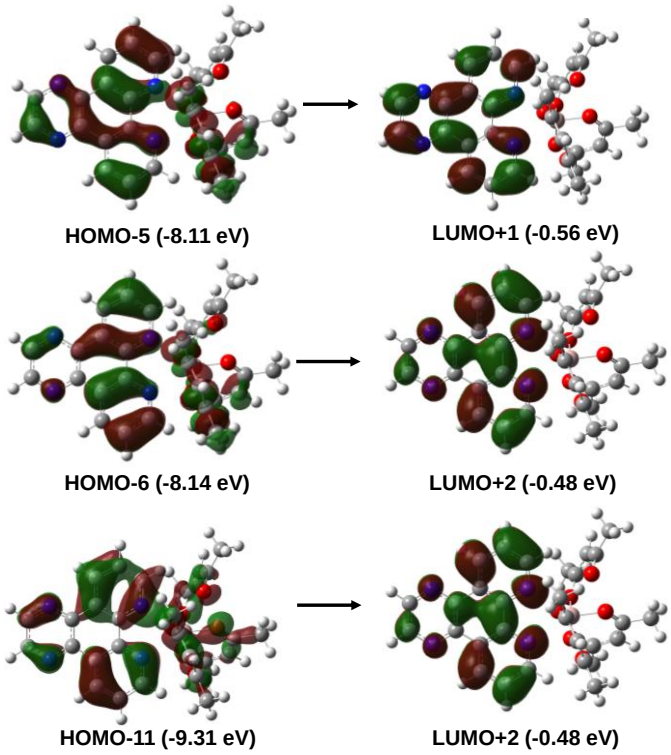

Fig. S6 Minor T_1 state configurations (5 %-10%) (HOMO-5→LUMO+1: 8 %, HOMO-6→LUMO+2: 6 %, HOMO-11→LUMO+2: 7 %).

S3. Coordination geometry of Tb(III) complexes in crystalline phase

Based on X-ray crystal analysis, the coordination sites of $Tb(acac)_3dpq$ and $Tb(tmh)_3dpq$ comprise three β-diketonate ligands and one dpq ligand with a hetero-π-conjugated system (Fig. S7). To determine the coordination geometry around the Tb(III) ion, we performed continuous shape measure calculations (Table S1).[14]

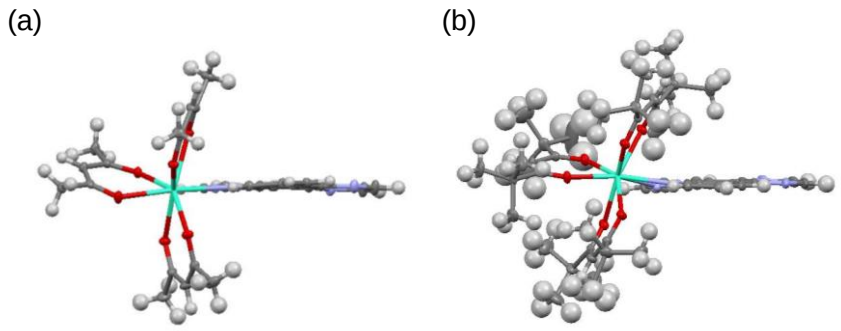

Fig. S7 Monomer unit in X-ray crystal structures of $Tb(acac)_3dpq$ and $Tb(tmh)_3dpq$

Table S1 S-factors of the Tb(III) complexes

		SAP(D_{4d})	TDH(D_{2d})	BTP(C_{2v})
$Tb(acac)_3dpq$	Solid	0.581	2.143	2.261
$Tb(acac)_3dpq$	Isolated	4.738	4.569	4.910
$Tb(tmh)_3dpq$	Solid	0.656	2.073	2.481

Unlike the similar steric unit structures between $Tb(acac)_3dpq$ and $Tb(tmh)_3dpq$ in a solid state, their aggregation forms are quite different. Two patterns of intermolecular dipole-dipole interactions (Fig. S8a, 1.0 nm (A-B) and 1.2 nm (A-C)) were observed for the $Tb(acac)_3dpq$ crystal structure, which corresponds to a slipped-cofacially stacked configuration, i.e., J-aggregation. In contrast, strong intermolecular π-π (Fig. S8b, 0.3 nm (A-B)) and weak dipole-dipole interactions (1.6 nm (B-C)) between the dpq ligands were observed for $Tb(tmh)_3dpq$, which corresponds to a face-to-face cofacial configuration, i.e., H-aggregation. Formation of this Tb-based H-aggregate is considered to arise from the large steric hindrance of the tmh ligands.

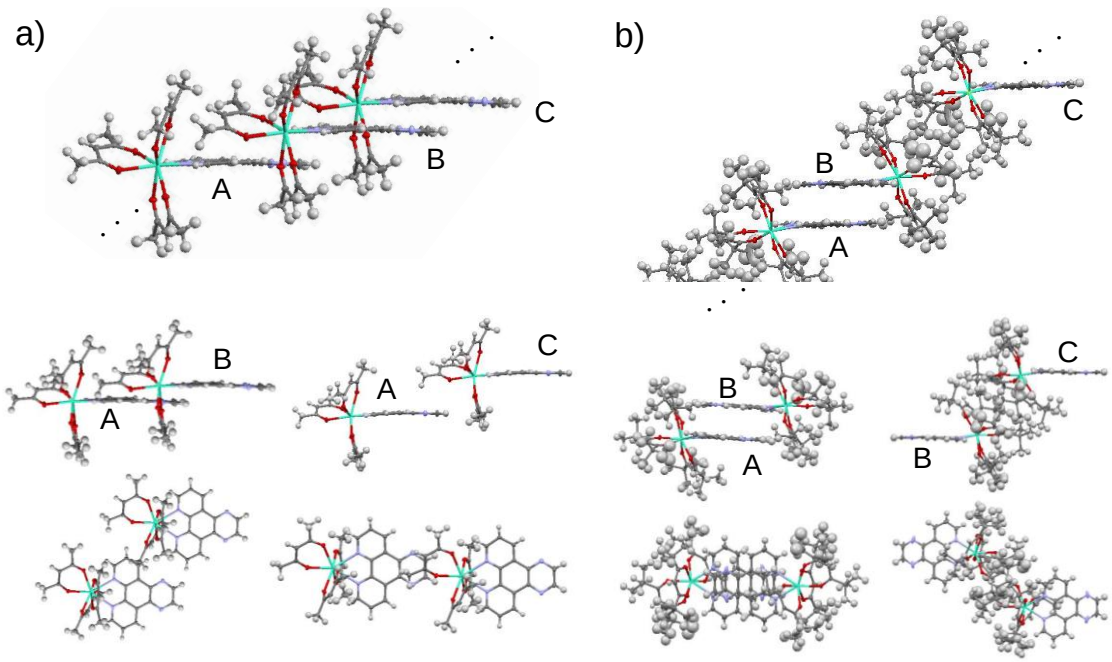

Fig. S8 ORTEP drawings (ellipsoids set at 50% probability) of $Tb(acac)_3dpq$ (a) and $Tb(tmh)_3dpq$ (b)

S4. TG-DTA of Tb(III) complexes in crystalline phase

The TGA profiles of $Tb(acac)_3dpq$ and $Tb(tmh)_3dpq$ are shown in Fig. S9. The thermostability of the J-aggregate is slightly higher than that of the H-aggregate, although the weight of the molecular units in the J-aggregate is less than that in the H-aggregate. The results indicate that J-aggregation forms a rigid structure, which enhances the thermostability.

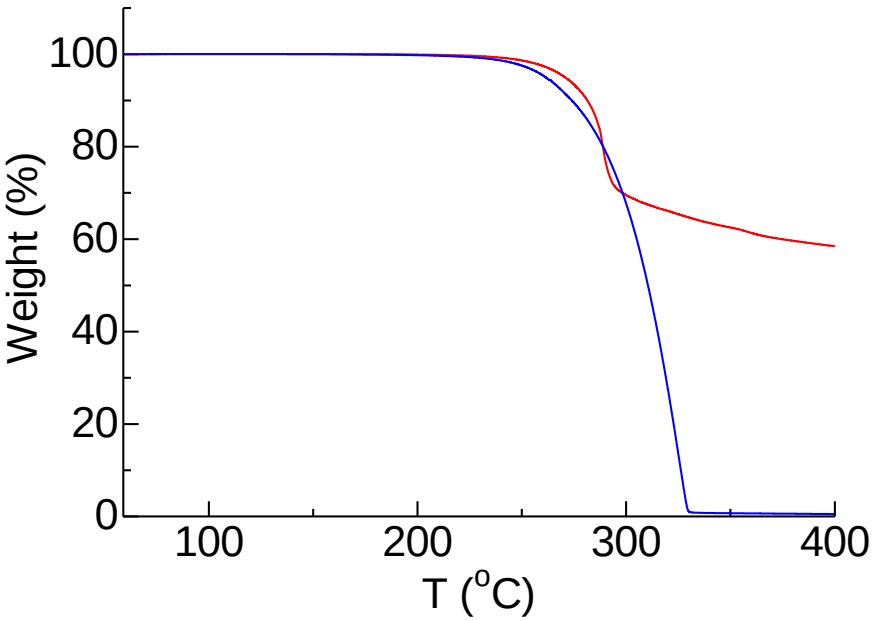

Fig. S9 TG-DTA of $Tb(acac)_3dpq$ (red line) and $Tb(tmh)_3dpq$ (blue line).

S5. Electronic absorption of Tb(III) complexes in solution and solid states

The electronic absorption spectra of dpq, $Gd(acac)_3dpq$ and $Gd(tmh)_3dpq$ in $CHCl_3$ are shown in Fig. S10. By the complexation, the electronic absorption bands were shifted from that of the free dpq ligand.

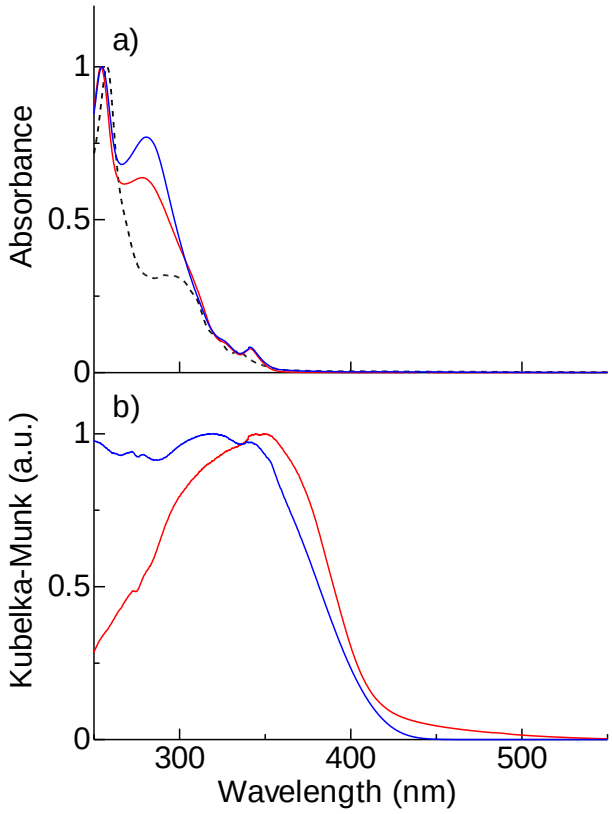

Fig. S10 Electronic absorption spectra of dpq in $CHCl_3$ (a, broken line, 2.0×10^{-5} M), $Tb(acac)_3dpq$ in $CHCl_3$ (a, red line, 1.1×10^{-5} M), in solid state (b, red line), and $Tb(tmh)_3dpq$ in $CHCl_3$ (b, blue line, 1.0×10^{-5} M), in solid state (b, blue line).

S6. DFT calculation of Tb(III) unit in solid states

To clarify the electronic structure of the ligand moieties in the Tb(III) complex unit in solid states, DFT calculations were performed on a simplified model of the Tb(III) unit using a ligand bonded to an Al(III) ion based on the single X-ray crystal structure (dpq: B3LYP/6-31+G(d, p), $Al(acac)_3$dpq: CAM-B3LYP/6-31G(d)). From the calculation results, the $S_0 \rightarrow S_1$ transition band can be ascribed to characteristic ligand-to-ligand charge transfer bands from β-diketonate to dpq ligands (Fig. S11). The energy donating states (T_1 state) of the dpq ligand and Tb(III) complexes were also calculated by TD-DFT (CAM-B3LYP/6-31G(d)). The T_1 state of the dpq ligand was estimated as 22700 cm^{-1}, which is similar to previous experimental values (23500 cm^{-1})[11a]. The formation of the Tb(III) complex caused almost no change in the T_1 energy (22900 cm^{-1}). The complex state is mainly composed of dpq localized excited states (Fig. S12).

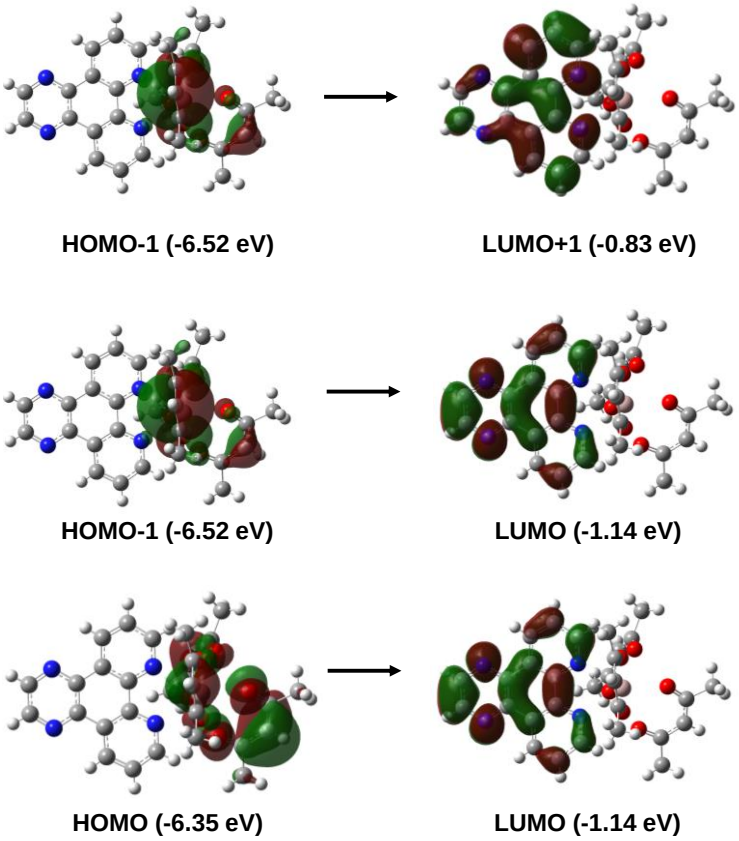

Fig. S11 Main S_1 state configurations (HOMO-1➔LUMO+1: 45 %, HOMO-1➔LUMO: 22 %, HOMO➔LUMO+1: 12 %).

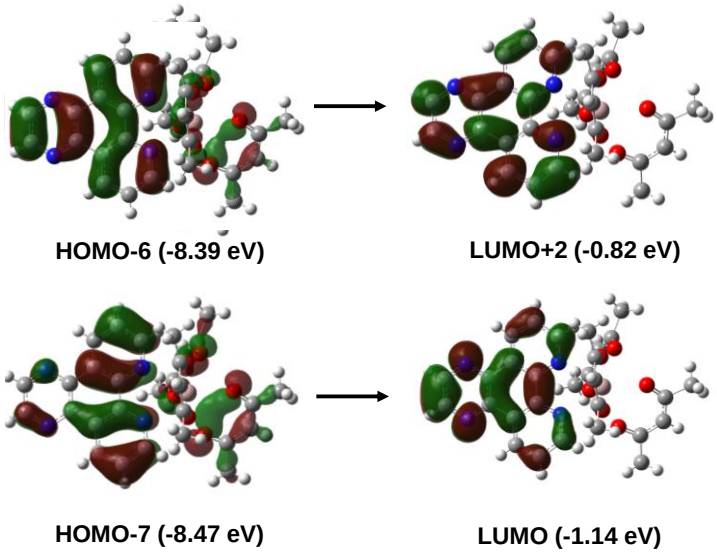

Fig. S12 Main T_1 state configurations (HOMO-6➔LUMO+2: 26 %, HOMO-7➔LUMO: 20 %).

S7. Crystal data and phosphorescence spectra of Gd(tmh)$_3$dpq and Gd(acac)$_3$dpq

A single crystal of Gd(tmh)$_3$dpq and Gd(acac)$_3$dpq was obtained by recrystallization from CH_2Cl_2/hexane solution. Although the structure of Gd(tmh)$_3$dpq is similar with that of Tb(tmh)$_3$dpq, the Gd(acac)$_3$dpq is different from that of Tb(tmh)$_3$dpq.

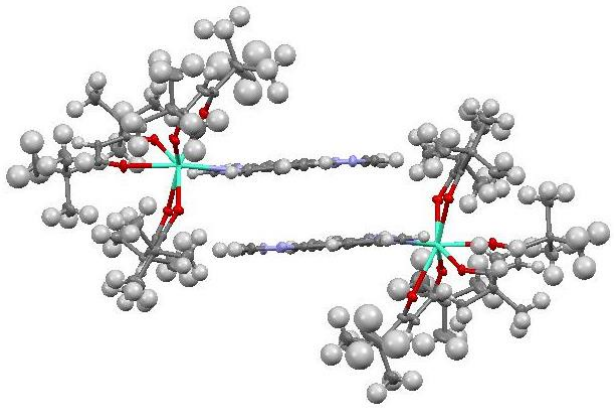

Fig. S13 Crystal structure of Gd(tmh)$_3$dpq.

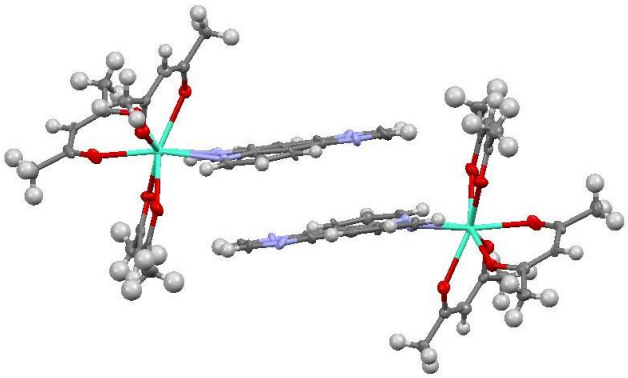

Fig. S14 Crystal structure of Gd(acac)$_3$dpq.

Table S2 Crystal data of $Gd(tmh)_3dpq$ and $Gd(acac)_3dpq$

	$Gd(tmh)_3dpq$	$Gd(acac)_3dpq$
chemical formula	$C_{47}H_{65}GdN_4O_6$	$C_{29}H_{29}GdN_4O_6$
formula weight	939.28	686.81
crystal system	monoclinic	monoclinic
space group	P 2_1/c	I 2/a
a / Å	13.4029(2)	14.962(2)
b / Å	15.2786(2)	17.893(4)
c / Å	26.4644(4)	23.016(5)
α / deg	90	90
β / deg	91.6930(10)	95.812(15)
γ / deg	90	90
volume /Å	5416.95(14)	6130(2)
Z	4	8
density / g cm^{-3}	1.152	1.488
Temperature / ºC	20	20
R	0.0337	0.0780
wR_2	0.1236	0.1576

S7. Emission and excitation spectra of CH-Tb(III)

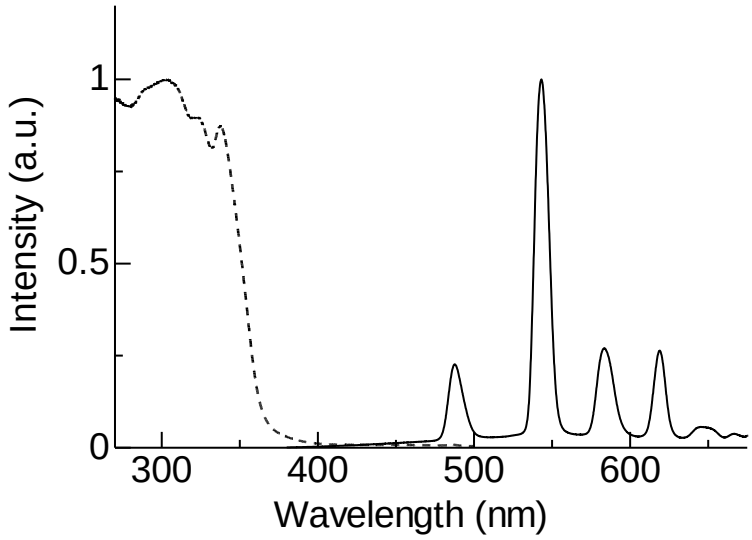

Fig. S15 Emission (solid line, λ_{ex} = 350 nm) and excitation (broken line, λ_{em} = 554 nm) of $Tb(tmh)_3dpq$ in solid state.

S8. Photophysical properties of $Tb(acac)_3dpq$ in solution and solid states.

We measured the emission spectra and time-resolved emission intensity of $Tb(acac)_3dpq$ (1.0×10^{-2} M) in non-degassed CH_2Cl_2 and degassed CH_2Cl_2 (Fig. S16), excited mainly by LLCT bands (Fig. S10-S11). The emission spectrum of $Tb(acac)_3dpq$ in non-degassed CH_2Cl_2 is almost the same as that in degassed CH_2Cl_2. The detected values for short emission lifetimes were also almost same (Fig. S17, $\tau_{non\text{-}degassed} = 4.3$ μs, $\tau_{degassed} = 5.1$ μs).

The emission spectrum in the solution state is relatively similar to that of CJ-Tb(III). This indicated that the radiative rate constants of $Tb(acac)_3dpq$ in solution are similar to those of CJ-Tb(III). Also, k_r and Φ_{ff} of Tb(III) complexes were calculated under the assumption that the emission lifetimes at 100 K (Fig. 8) are the radiative emission lifetimes (τ_{rad}).[S2-S3] CJ-Tb(III) also exhibited a relatively high Φ_{ff} of 62%, a high k_r (1.4×10^3 s^{-1}), and a relatively small k_{nr} (8.6×10^2 s^{-1}). On the other hand, $Tb(acac)_3dpq$ in solution exhibited a low Φ_{ff} of 0.6% and a high k_{nr} (2.3×10^5 s^{-1}), under the assumption that the radiative rate constants of $Tb(acac)_3dpq$ in solution are the same as those of CJ-Tb(III). The calculation assumes that solidification strongly suppresses the non-radiative process of $Tb(acac)_3dpq$.

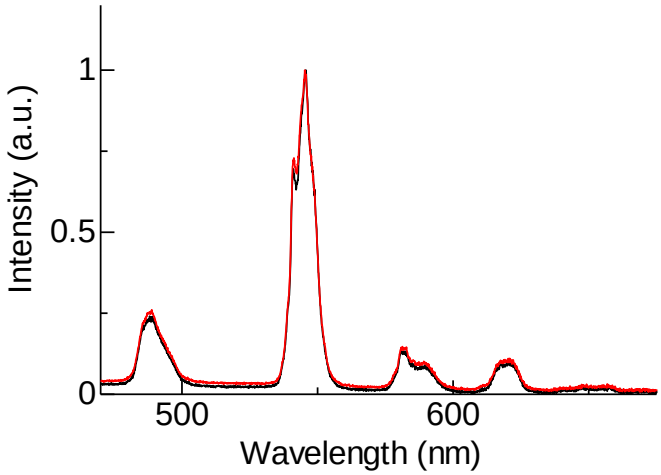

Fig. S16 Emission spectra of Tb(acac)$_3$dpq in non-degassed CH_2Cl_2 (1.0×10^{-2} M, black line) and degassed CH_2Cl_2 (1.0×10^{-2} M, red line).

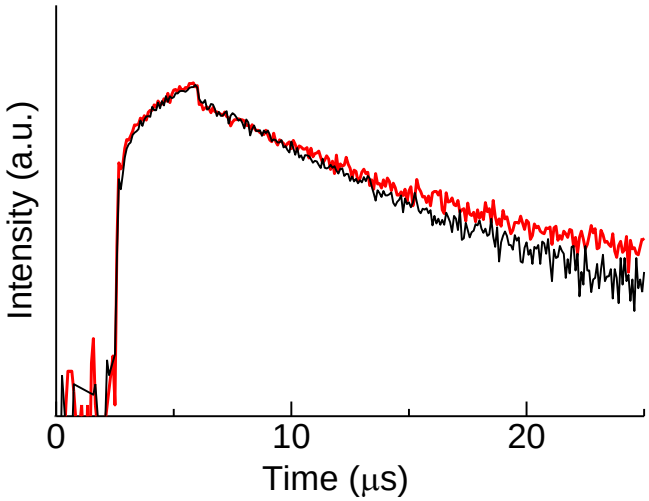

Fig. S17 Emission decay curves of Tb(acac)$_3$dpq in non-degassed CH_2Cl_2 (1.0×10^{-2} M, black line) and degassed CH_2Cl_2 (1.0×10^{-2} M, red line).[S4]

S9. AIE property using other solvents

We investigated the AIE behavior of CJ-Tb(III) using $CHCl_3$ and $C_2H_4Cl_2$ (1,2-dichloroethane) as solvents (1.0×10^{-3} M). In $CHCl_3$ and $C_2H_4Cl_2$ solutions, $Tb(acac)_3dpq$ showed emission bands originating from the Tb(III) ion (Fig. S18). After solidification by a casting solution, we observed bright emissions (Fig. S19) for solid Tb(III) complexes, although $Tb(acac)_3dpq$ in the solutions showed very weak emissions. Their emission lifetimes in the solid states were different (τ_{ave}(cast-$CHCl_3$) = 0.39 ms, τ_{ave}(cast-$C_2H_4Cl_2$) = 0.43 ms, Fig. S20). Therefore, these results indicate that the AIE property is solvent-dependent.

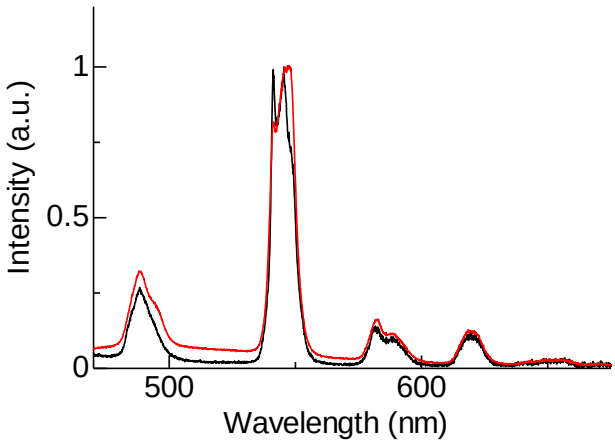

Fig. S18 Emission spectra of $Tb(acac)_3dpq$ in $CHCl_3$ (1.0×10^{-3} M, black line), $C_2H_4Cl_2$ solution (1.0×10^{-3} M, red line).

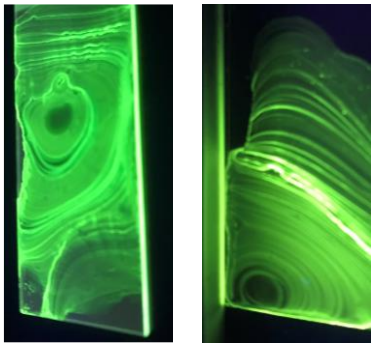

Fig. S19 Photograph of solid $Tb(acac)_3dpq$ obtained by casting solution ($CHCl_3$ and $C_2H_4Cl_2$).

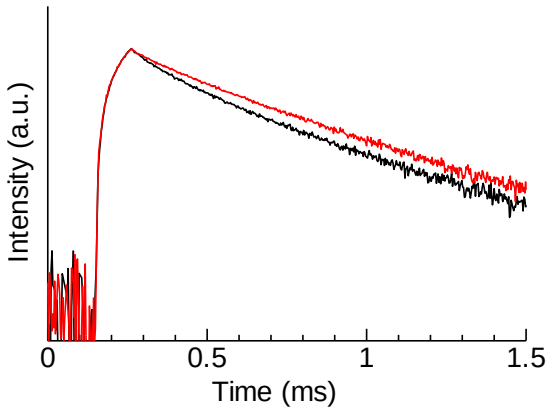

Fig. S20 Emission decay curves of $Tb(acac)_3dpq$ in solid state prepared by casting solution ($CHCl_3$: black line, $C_2H_4Cl_2$: red line).

S10. Emission decays of CJ-Tb(III) excited by Tb(III) ion

The emission lifetime of CJ-Tb(III) excited by ligands (0.47 ms) was same with that of excited by Tb(III) ion (0.47 ms), indicating the energy transfer rate is higher than the deactivation rate from Tb(III) emitting level.

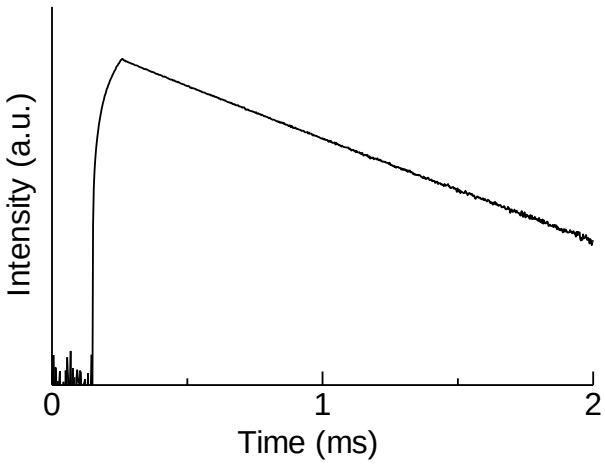

Fig. S21. Emission decays of CJ-Tb(III) excited by ligands (356 nm).

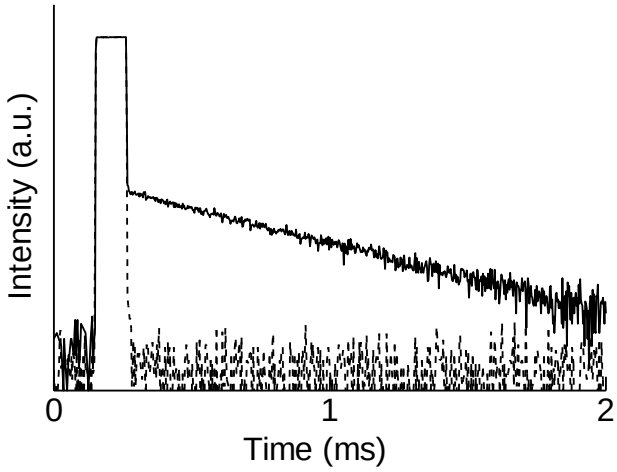

Fig. S22 Emission decays of CJ-Tb(III) excited by Tb(III) ion (495 nm) (black solid line: Tb(III) emission, black broken line: prompt).

S11. TEM measurement of $Tb(acac)_3(dpq)$-SDS

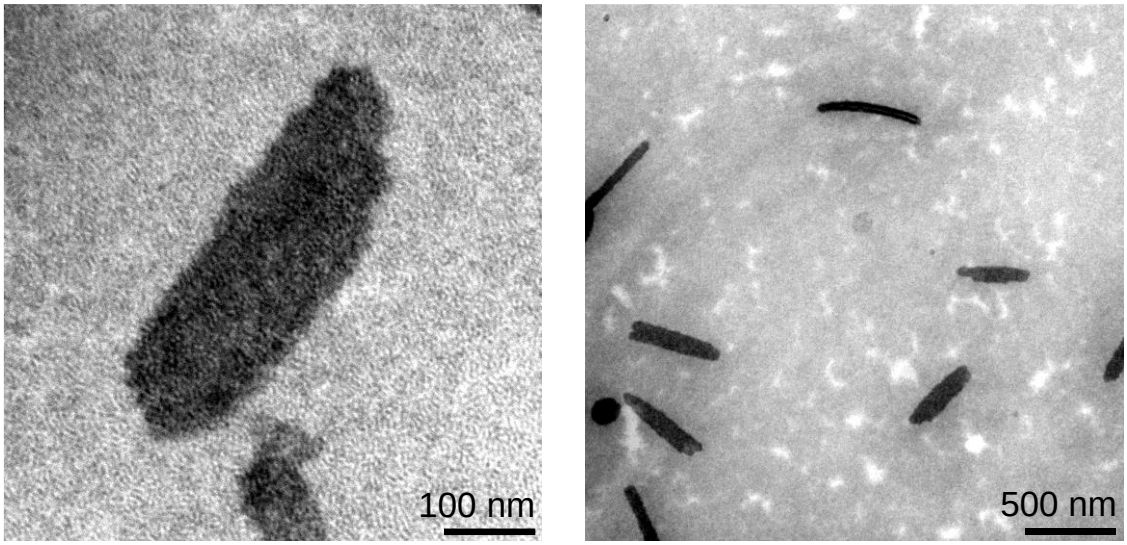

Fig. S23 TEM images of $Tb(acac)_3(dpq)$-SDS (JEM-2010, 200 kV).

References and Notes

S1. S. Quici, M. Cavazzini, G. Marzanni, G. Accorsi, N. Armaroli, B. Ventura and F. Barigelletti, *Inorg. Chem.* 2005, **44**, 529.

S2. R. Pavithran, N. S. S. Kumar, S. Biju, M. L. P. Reddy, S. A. Junior, R. O. Freire, *Inorg. Chem.* 2006, **45**, 2184.

S3. K. Yanagisawa, T. Nakanishi, Y. Kitagawa, T. Seki, T. Akama, M. Kobayashi, T. Taketsugu, H. Ito, K. Fushimi and Y. Hasegawa, *Eur. J. Inorg. Chem.* 2015, **28**, 4769.

S4. We can also detect the weak, longer lifetime components; however, we cannot determine the origin of these components at present although they might originate from the AIE component in solution or a part of the dissociation complex.